Spatiotemporal maturation patterns of murine brain quantified by diffusion tensor MRI and deformation-based morphometry

Ragini Verma*, Susumu Mori[†‡], Dinggang Shen*, Paul Yarowsky[§], Jiangyang Zhang[†], and Christos Davatzikos*[¶]

*Section of Biomedical Image Analysis, Department of Radiology, University of Pennsylvania, 3600 Market Street, Suite 380, Philadelphia, PA 19104; [†]Department of Radiology and [‡]Center of Magnetic Resonance Microimaging, The Johns Hopkins University School of Medicine, 217 Traylor Building, 720 Rutland Avenue, Baltimore, MD 21205; and [§]Department of Pharmacology and Experimental Therapeutics, University of Maryland, Room 4-021 Bressler Research Building, 655 West Baltimore Street, Baltimore, MD 21201

Edited by Leslie G. Ungerleider, National Institutes of Health, Bethesda, MD, and approved March 23, 2005 (received for review October 20, 2004)

Highly heterogeneous spatiotemporal patterns of maturation of the murine brain during the first 80 postnatal days were examined by high-dimensional deformation-based morphometry applied to high-resolution diffusion tensor MRIs. The maturation profile revealed a sharp contrast between tissue anisotropy changes in the cortex and in major white-matter fibers. Radially oriented tissue anisotropy was measured during the first postnatal week in cortical regions, reflecting the underlying columnar organization of the cortex. Subsequently, tissue anisotropy reduced rapidly, potentially reflecting the growth of randomly oriented dendritic trees that reduce tissue coorientation. Distinct anisotropy patterns were also observed along layer I of the cortex and were attributed to thin fibers oriented parallel to the outer surface. Last, spatially complex patterns of maturation were measured in all major axonal pathways and in the hippocampus, caudate putamen, and cerebellum. This analysis provides a framework for quantifying normative maturation patterns against which phenotypes of mice of different genetic and environmental backgrounds can be contrasted.

Postnatal brain development in the mouse presents spatiotemporal patterns of growth and myelination that vary rapidly in the early postnatal days, reaching a plateau toward adulthood. Detailed quantification of morphological changes occurring during this dynamic process is important not only for understanding normal development but also for contrasting it to disturbances caused by a variety of genetic or environmental factors (1, 2). The complex nature of the dynamic changes occurring during the early postnatal period requires the use of sophisticated quantitative analysis approaches that are capable of capturing complex spatiotemporal patterns and large changes in size due to growth. This study provides a method for quantification and visualization of spatiotemporal maturation patterns of the murine brain by using high-resolution diffusion tensor imaging (HR-DTI) and deformation-based morphometry (DBM), and we used it for analysis of maturation profiles during the first 80 postnatal days.

MRI offers the potential for large-sample studies because of the relatively low human effort that is involved. It is also largely free of distortions and sectioning artifacts. Thereby, MRI complements histological staining methods and can serve as a hypothesis generation method for focused histological and molecular examinations (3–7), as well as for longitudinal studies of development, disease progression, or effects of pharmacological interventions. Studies on mice using MRI (6–8) are based primarily on adult mice. The MRI modalities used by these studies do not offer adequate tissue contrast during early postnatal ages. However, contrast in HR-DTI (9, 10) enables identification of various brain structures, including axonal pathways, even during embryonic stages (11–14) and in small animals (15–18). HR-DTI exploits the fact that the characteristics of tissue microstructure affect the microscopic diffusion of water molecules within it, as reflected by a parameter called fractional anisotropy (FA) ranging from 0 to 1 (see Figs. 1 and 3). Directionally restricted water diffusion is called anisotropic (FA is high), and diffusion without directional constraint is said to be isotropic (FA is low). Gray matter (GM) in the brain is relatively isotropic in adult mice, whereas the white matter (WM) is anisotropic, primarily arising from the alignment of ordered myelinated axons, which preferentially constrain water diffusion along the axonal direction. In fetal and early postnatal tissue, water diffusivity can also selectively increase along neuronal processes and cortical layers arranged in columnar organizations, as well as along the spatially cooriented glial scaffolding during neuronal migration from the subventricular zone to the cortex. Thus, by exploiting the mechanism of diffusion and the physical microstructure of WM tissue, HR-DTI provides a means of imaging the neural pathways critical in studying brain connectivity, as well in understanding how genetic mutations affect the formation, myelination, or degeneration of axonal fibers.

Although specific regions of interest (ROIs) can be drawn on DTIs to measure the overall growth and maturation of structures such as the cortex, caudate putamen (cpu), cerebellum, and major axonal fiber bundles, the complex spatiotemporal patterns of the developing murine brain cannot be fully captured by such gross morphometric measurements. In this study, we overcame this limitation by using deformation-based analysis, which does not rely on any *a priori* definitions of ROIs but examines the spatiotemporal pattern of morphological characteristics throughout the entire brain. Deformation-based techniques recently have been shown by other related studies to capture complex spatial patterns of brain development in humans both in normal populations (19–21) and in adolescents with early-onset schizophrenia (22). This study uses it for temporal analysis of murine brains in conjunction with HR-DTI.

We employ high-dimensional elastic deformations to map the anatomy of the murine brain at a given age to its configuration at another age, a process that enables direct calculations of growth and myelination at comparable spatial and image resolution. As a result, we observed spatially complex and highly localized patterns of brain changes in tissue anisotropy involving both cortical and subcortical structures. It is important to note that biases could be introduced if manually placed anatomical landmarks were used to find the aforementioned spatial trans-

This paper was submitted directly (Track II) to the PNAS office.

Abbreviations: ROI, region of interest; DTI, diffusion tensor imaging/image; HR-DTI, high-resolution DTI; FA, fractional anisotropy; DBM, deformation-based morphometry; GM, gray matter; WM, white matter; ic, internal capsule; ec, external capsule; ac, anterior commissure; cpu, caudate putamen; hpc, hippocampus; cc, corpus callossum; dhc, dorsal–hippocampal commissure; vhc, ventral–hippocampal commissure.

[¶]To whom correspondence should be addressed. E-mail: christos@rad.upenn.edu.

www.pnas.org/cgi/doi/10.1073/pnas.0407828102

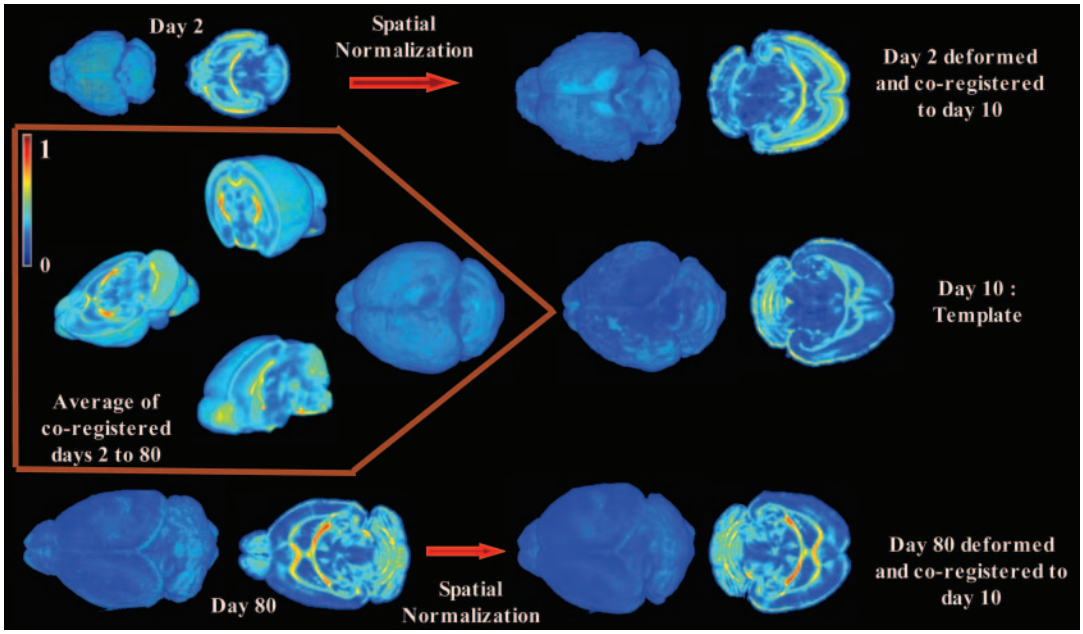

Fig. 1. Visualization of spatial coregistration. The 3D volume-rendered FA maps of three representative murine brains of ages 2, 10, and 80 days (postnatally) are color-coded (red, high; blue, low) to show the internal anatomy. Red arrows show renditions of their deformed versions. After coregistration, all deformed images were averaged to form the image rendered in *Inset*, along with sections revealing internal structures displaying high average FA across different ages.

formations. We avoid such biases by using a fully automated image deformation technique (23) that performs computerized anatomical pattern matching among different mouse images to obtain a dense map from one anatomy to another, which is necessary for capturing subtle morphological characteristics beyond a limited number of landmarks or ROIs. This previously extensively validated image deformation process (24–27) is highly objective because it has no human involvement.

The result of our study is a dynamic map of the spatiotemporal heterogeneity of brain development and maturation, revealing a sharp contrast between maturation of the cortex and that of major WM fibers, with the cortex initially displaying high tissue anisotropy along the radial direction that rapidly decreases during the first postnatal week, and the WM fibers displaying an opposite trend. The cortical maturation pattern is believed to be due to the transition from spatially radially cooriented neuronal cell bodies to less oriented tissue, as dendritic trees elaborate and synaptic density increases, whereas the fiber maturation pattern is attributed to growth and myelination of major axonal pathways. However, additional studies comparing imaging findings with histological analysis are necessary to confirm precisely which underlying maturation processes lead to the observed MR signal changes. Analogous patterns were observed in the hippocampus (hpc), in which the initial high FA values can be attributed to early laminar organization of cell body layers of interneuronal connections, followed by lower FA values as dendritic and synaptic formations increase with age. Similarly, patterns were observed in the cerebellum showing steadily increasing FA values because of the postnatal development of the granule cell layer and WM maturation. Importantly, this dynamic map is not restricted to visual and qualitative evaluation of brain development, but it provides quantitative spatiotemporal measurements of normal brain development against which similarly constructed spatiotemporal maps of other wild-type or neurogenetic mice can be compared quantitatively by using the methodological approach described here.

Methods

HR-DTI scans were acquired from mouse brains (C57BL/6J) of various postnatal developmental stages. Postnatal brain development is more pronounced in the first 3 weeks, although considerable changes can occur up to 8–12 weeks postnatally. Therefore, we sampled the period of day 1–80 nonlinearly, choosing days 2, 5, 7, 10, 15, 20, 30, 45, and 80 for our analysis and acquiring a single sample at each time point. C57BL/6J is an inbred strain, and these mice are considered to be genetically equivalent and, hence, appropriate for such a study.

Mouse Data: DTI Acquisition and Processing. Mouse specimens were fixed by using 4% paraformaldehyde in PBS for >1 month. Before imaging, they were transferred to custom-built MR-compatible tubes filled with fombin, to prevent dehydration. DT imaging was performed by using GE Omega 400 unit (9.4 T; General Electric) equipped with triple-axis gradients. A custom-made solenoid volume coil was used as both the radio frequency signal transmitter and receiver. The NMR sequence was based on a 3D multiple echo sequence with navigator echo phase correction scheme and segmented *k*-space acquisition (28). At least seven diffusion-weighted images were acquired with a repetition time of 0.9 s, an echo time of 37 ms, and two signal averages, with the total imaging time being 24 h. They were acquired with different b values ranging from 150 to 1,200 s/mm^2. The field of view ranged between $12 \times 6 \times 6$ mm^3 for the smallest (day 0) to $17 \times 11 \times 8$ mm^3 for the largest. The imaging matrix had dimensions from $128 \times 70 \times 64$ to $128 \times 84 \times 80$, which was zero-filled to double their sizes after the spectral data were apodized by a 10% trapezoidal function. The native imaging resolutions ranged from $93 \times 93 \times 93$ to $120 \times 120 \times 120$ μm. All experiments were approved by the Animal Research Committees of The Johns Hopkins University and the University of Pennsylvania.

Diffusion tensors were fitted to each voxel in the image by a process of multivariate linear fitting on the diffusion-weighted images acquired at various gradient directions (9, 10). Unlike 3D scalar images, each voxel in the DT image contains a tensor, represented by a 3×3 symmetric positive definite matrix having six independent elements. From the diffusion tensor, three eigenvalues and their corresponding eigenvectors were calculated. The vectors represent the direction of diffusivity, and the

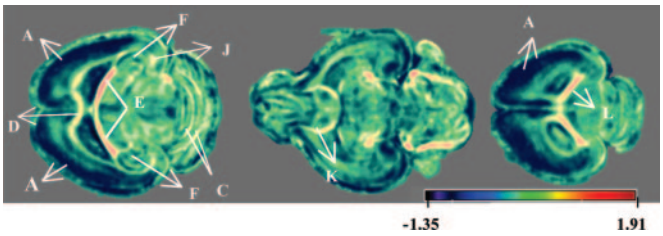

Fig. 2. Color-coded maps of rate of change of FA per day, obtained by regression on spatially coregistered mouse brains from days 2–80. The regions of special interest that show a large change in FA are as follows: A, cortex; B, ec; C, fissures of the cerebellum; D, genu of cc; E, ic; F, hpc; G, vhc; H, cpu; J, dhc; K, ac; and L, splenium of cc. The color coding shows, in the 80 days, the FA of the cortex, cpu, and hpc is reduced, whereas the FA of the ic and ec, splenium, and genu of the cc and ac increases.

eigenvalues λ_1, λ_2, and λ_3 represent the magnitude of diffusivity in the three principal directions. By using these eigenvalues and the mean diffusivity $\bar{\lambda}$, the FA was calculated to yield values of 0–1:

$$\mathrm{FA} = \sqrt{\frac{3}{2}}\,\frac{\sqrt{(\lambda_1-\bar{\lambda})^2+(\lambda_2-\bar{\lambda})^2+(\lambda_3-\bar{\lambda})^2}}{\sqrt{\lambda_1^2+\lambda_2^2+\lambda_3^2}}.$$

An image created with FA values corresponding to each voxel is called the FA map. These FA maps reveal various brain structures, many of which are shown in Figs. 2 and 3 (29). Also, the map (vector field) in which each voxel is assigned the principal eigenvector is the orientation map of the DT image (9, 10, 30).

Spatial Normalization of DT Images Using Elastic Deformations. We constructed the temporal profile by using the FA and orientation maps of the DT images acquired at different developmental stages. We spatially coregistered images of all days to a common template, thereby enabling subsequent region by region comparisons throughout the entire brain. We selected the brain of day 10 as a template because it is a midway sample in terms of time and growth process. We repeated all of the experiments (regression analysis and difference between various stages of development) with the brain of day 15 as the template, and we found nearly identical results to those using day 10 as a template (Fig. 6, which is published as supporting information on the PNAS web site). Fig. 1 shows the 3D volume-rendered murine brain before and after spatial normalization for days 2 and 80. The same procedure was applied to brains at other developmental stages, and an average was created, which is shown in Fig. 1 *Inset*.

We coregistered the DT images by first normalizing the FA maps and then using that deformation to reorient the DT images. The FA maps were coregistered elastically with the template by hierarchically matching features that provide a rich morphological signature for each voxel, distinctive on points with same FA value with different anatomic context (23, 31, 32). These features are based on local spatial-intensity histograms of multiresolution images around each point combined with the edge information. The elastic registration transformation reconfigures the anatomy at all time points to the template (23, 32). These displaced tensors are reoriented by using the underlying rotation component of the transformation, computed by a locally adaptive Procrustes estimation (33, 34), producing a coregistered DT image. Reorientation is a very important step that is not encountered in processing of conventional scalar images.

The image warping algorithm used for the FA maps has been extensively validated and applied to various imaging problems, including structural and functional studies of development, aging, dementia, and effects of sex and genotype on the brain (25–27, 35). Notably, this study applies the method to FA maps, which because of the inherent noise are difficult to register with existing routines that depend on the segmentation of the brain into WM, GM, and CSF. We further validated the algorithm on FA maps by comparing the registration accuracy against the accuracy of landmark identification by human raters and found no significant difference between these measures of accuracy. Also, the clarity of the average images is one visual indicator of the correct alignment of structures and, hence, of good coregistration of the spatially normalized images.

Results

Having established a fully automated DBM method for analyzing HR-DTI of murine brains, we used it to perform a multi-

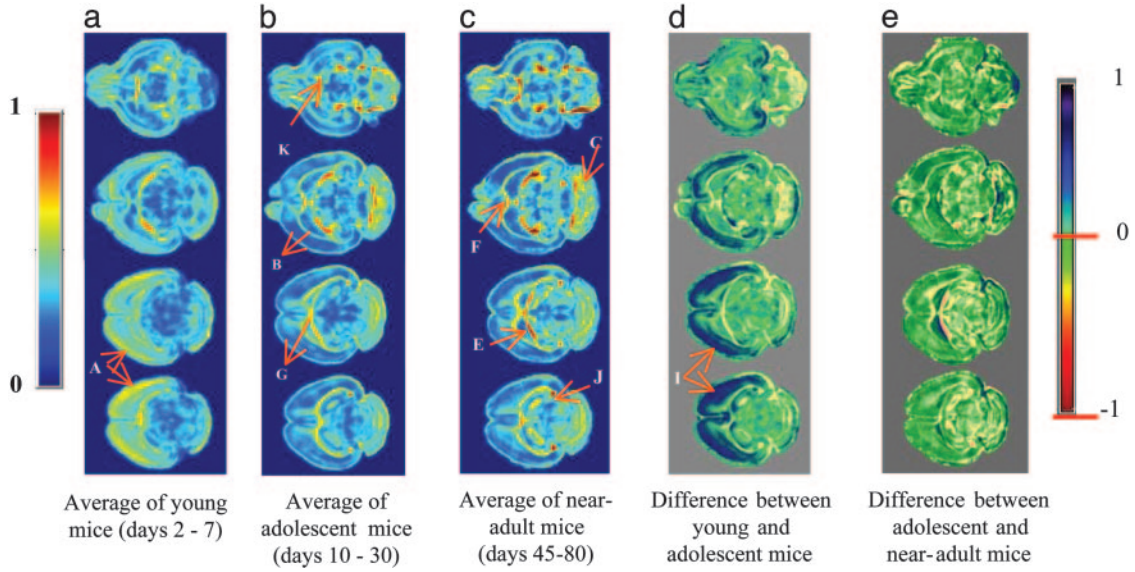

Fig. 3. Average and difference maps of FA. (*a–c*) Various slices from the average maps of the young (before day 10), adolescent (days 10–45), and near-adult mice (beyond day 45). (*d*) The difference between the young and adolescent mice. (*e*) The difference between adolescent and near-adult mice. The slices shown are 58, 80, 95, and 102, in which the total brain is represented by a 280 × 280 × 140 image. The left color bar is for *a–c*, and the right bar is for *d* and *e*.

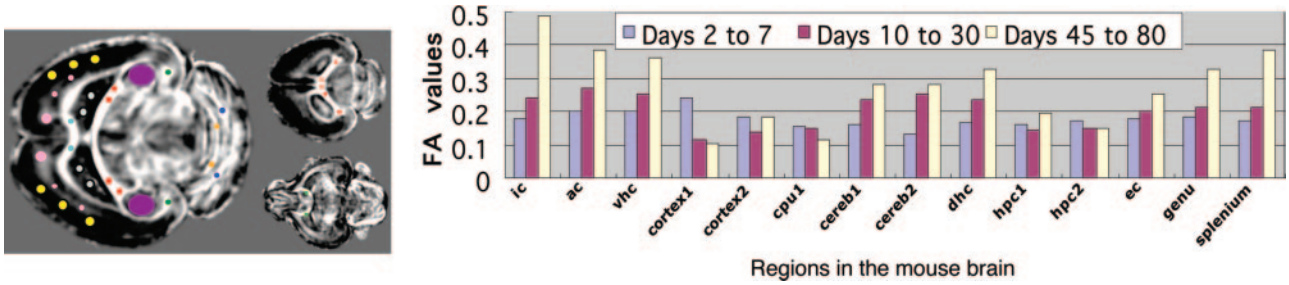

Fig. 4. Regional changes in FA value in the three developmental stages of young, adolescent, and near-adult mice (see Fig. 3). The following marked regions (see Fig. 2) were used to sample several structures and graph their temporal change: ic, ac, vhc, cortex (2 regions), cpu, fissures of the cerebellum (cereb1 and cereb2), dhc, two regions in the hpc (hpc1 and hpc2), ec, and the genu and the splenium of the cc. The graphs show the nonlinear regression maps of each of the regions.

faceted analysis on these spatially normalized FA maps. We constructed the temporal maturation profile of the 80 days by jointly analyzing all FA images on a voxel-by-voxel basis by using regression with age (a voxel is the smallest spatial unit in a 3D image volume, the 3D analog to a pixel). Also, we studied differences between different developmental stages. We graphed regional developmental patterns over time by sampling the temporal pattern of FA change in several regions of the brain.

Temporal Maturation Profile. The voxel-wise regression map of the coregistered FA maps from day 2–80 is shown in Fig. 2 sampled at different planes. Fig. 2 shows significant decrease in anisotropy in cortex and in certain layers of the hpc, with the decrease being more pronounced toward the outer layers but not along the outermost cortical layer. It also shows a pronounced increase of the FA in most major WM fiber pathways, including the internal capsule (ic), the genu, and the splenium of the corpus callossum (cc), the anterior commissure (ac), the dorsal–hippocampal commissure (dhc), the ventral–hippocampal commissure (vhc), and layers of the cerebellum. A localized decrease in anisotropy of the cpu is pronounced at the superior aspect of it, which is where the thalamo-cortical axons project.

To measure the change in tissue anisotropy with development, we assigned the mice into the following three different stages: young (before day 10), adolescent (days 10–45), and near-adult (after day 45). To study the growth difference between these stages, we averaged the spatially normalized FA maps within each of these stages. The color-coded average maps are shown in Fig. 3 *a–c*. The difference maps in 3 *d* and *e* show anisotropy changes between these developmental stages. The following structures are highlighted to stress their pronounced maturation profiles: layers of the cortex displaying strong anisotropy in young age (A) and then decreasing rapidly, as shown by the difference maps (I); maturation of ic and vhc (E); and maturation of cerebellum (C), dhc (J), ac (K), and cc (F). The cortical maturation pattern was not very localized, because it spanned large areas of primary motor, visual, and auditory cortices, especially along the outer cortical layers, except for the outermost cortical layer. However, note that it did not show significant spread outside these areas and did not extend to ventral cortical regions.

Regional Patterns of Change in Tissue Anisotropy. To graph the temporal changes of tissue anisotropy within several representative brain structures, we sampled the regions shown in Fig. 4. Because the structural complexity of the hpc made it difficult to sample a smaller region, we placed a larger mask as shown in Fig. 4, with the understanding that more localized variations are present within the hpc, as shown in Figs. 2 and 3. The following two cortical regions are shown in Fig. 4: "cortex1" (yellow) regions change rapidly during the first postnatal week, and "cortex2" (pink) regions display relatively more gradual decrease in FA. The cc shows a steady increase with age, with the genu displaying a relatively more rapid increase. The ic and ac show a gradual increase with time, whereas the dhc displays very pronounced maturation changes. The adjacency of dhc to the cingulum makes it impossible to separate the maturation patterns of these two structures from each other. However, after carefully examining the entire set of slices (data not shown), especially along the rostral–caudal direction, we concluded that the pronounced maturation pattern in that region must be primarily due to the dhc. The FA value in the cpu gradually decreases with age at the superior aspect of cpu, where thalamocortical projections abound. The FA value in the hpc decreases with age, albeit gradually; however, the different layers of the hpc showed different maturation rates, as shown in Fig. 2. Region-wise regression maps of FA are presented in the graphs in Fig. 7, which is published as supporting information on the PNAS web site.

We show the percentage of change in FA in Table 1, for some major structures. In addition to these structures, we found that the cpu showed a more gradual decrease than the cortex. The two regions in the hpc showed differential FA changes depending on where the ROIs were defined because of the laminar structures within.

To address the issue of reproducibility and variability, we repeatedly sampled the regions described above and graphed the average of the FA values of these multiple selections. To account for potential misregistration errors in the deformation process, we also defined the same ROIs on the average of all spatially normalized images, instead of the day 10 template. We found a pattern of change that was similar to those in the graphs in Fig. 4, further bolstering our confidence in the results.

In Figs. 2 and 3, a layered and differential maturation of the cortical layers is shown. To examine the orientation of the underlying tissue structure that causes this differential change,

Table 1. Change in FA during the developmental stages of young, adolescent, and adult mice

Structure	Changes between young and adolescent mice	Changes between adolescent and old mice
Internal capsule	33% increase	88% increase
Anterior commissure	36% increase	42% increase
vhc	26% increase	41% increase
dhc	43% increase	39% increase
Cortex 1	52% decrease	Gradual decay
Corpus callossum	54% increase	82% increase

Developmental stages are as described in the text.

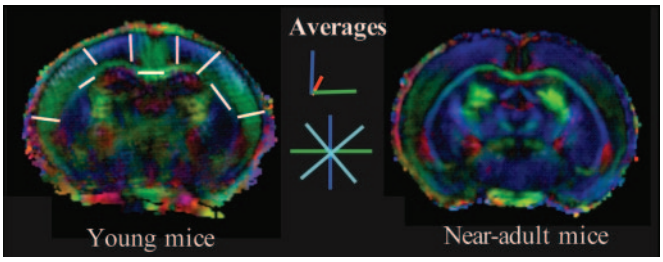

Fig. 5. Average of coregistered DT images of young and near-adult mice (see Fig. 3) color-coded according to tissue directionality. White lines in *Left* are representative samples from this orientation map, many of which reflect the radial orientation of cortical tissue, and others the orientation of fiber bundles. The orientation does not change much in *Right*, albeit the FA, represented by the color intensity, decreases in the cortex and increases in WM fibers, which can be attributed to formation of randomly oriented cortical dendritic trees and fiber maturation processes, respectively. Note that cyan, having equal blends of blue and green, corresponds to diagonal orientations. Red reflects orientation perpendicular to the image plane.

we spatially normalized the DTIs and generated the orientation color map using their principal eigenvector maps (10, 36), which reflect the underlying tissue orientation. Because 3D orientation cannot be easily displayed on 2D images, we used a standard color-coding scheme (36) that uses green, blue, and red along the three orthogonal directions shown in Fig. 5; color blends represent intermediate orientations. Fig. 5 shows slices from the color-orientation maps of the average of the DT images from days 2–7 and after day 45. The cortical layers and the WM structures, such as the cc, ic, and external capsules (ec), are clearly visible in the form of a vector color map.

Discussion

Our data support the hypothesis that DBM in conjunction with HR-DTI can quantify dynamic patterns of change in tissue anisotropy due to brain maturation and measure patterns of high spatial and temporal heterogeneity. Very early postnatal cortical maturation (days 2–7) was measured by decreasing FA values, and it stabilized by day 10. This maturation path is likely to reflect the underlying dendritic tree elaboration and synaptic density increase. In young postnatal mice, dendrites are not as fully developed, and the dendritic spines along the apical shafts of pyramidal cells are few (37). Radial morphology of dendrites, neuronal cell-bodies, axons, and glia at this stage results in a high FA value, as well as in radially oriented tensors (Fig. 5). As the dendritic tree matures and dendritic spines develop, dendritic trees do not present strong orientation preference analogous to the radial orientation of neuronal cell bodies and glia, thereby leading to reduced FA values. The outer cortical layers, except the most superficial layer I, displayed a nearly 50–60% drop in anisotropy in primary motor, sensory and auditory areas. Before stabilizing, the inner cortical layers showed a gradual consistent decrease of 20–25%. The cpu and hpc also displayed a gradual decrease in anisotropy in the range on 10–20%. In contrast, a steady increase in FA of major axonal fibers was measured on days 2–80. This rate of maturation was quite heterogeneous throughout the brain, with the ic and the dhc displaying the fastest maturation rate with a total change in FA approaching 100% during the first 80 days. In the cc, the genu and the splenium underwent an increase in anisotropy, with the splenium displaying a greater change in the range of 80–100%. These WM fibers generally displayed relatively modest to high early postnatal FA values, which was mainly attributed to tightly packed axons that allow water diffusion primarily along the fiber directions. Subsequently, they displayed rapid changes with increasing age, which could perhaps be attributed to further formation and myelination of axons, that further restricts transverse diffusion and could lead to an increase in tissue anisotropy. The cerebellar layers also displayed a strong, albeit somewhat delayed, maturation pattern.

The cortical changes were pronounced during the first postnatal week and stabilized afterward, displaying a very characteristic spatial pattern mainly spanning primary motor, sensory, and auditory cortical areas. Moreover, cortical FA signal changes tended to be localized primarily along the middle to superficial cortical layers, with notable exception of the most superficial (outermost) cortical layer. Specifically attributing this distinct maturation pattern to underlying cellular processes is beyond the capabilities of DT-MRI, especially in view of the complexity and variability of the neuronal cells and their connections and in view of the complexity of the processes governing axonal and dendritic development and maturation. However, the observed pattern is in agreement with the overall microstructural organization of the cortex, as well as with the development of dendritic trees whose random spatial orientation is likely to be the main cause of the reduction of the value of FA in the DTIs. However, in the early postnatal days, the radial orientation of cell bodies and many of their axons gives rise to increased FA (37, 38). The orientation maps of Fig. 5, showing a clearly radial orientation of the tissue that displays high FA, further bolster our confidence that increased FA values in days 2–7 are indeed due to radially oriented tissue.

Note the high anisotropy along the outermost cortical layer, which is known to comprise mainly thin fibers and glia, giving rise to highly oriented tissue. The sparsity of neuronal cell bodies along that layer I of the cortex (39) limits dendritic formation reflected by the stability of the FA with increasing age. Deeper layers, especially in the vicinity of layers II and III of the cortex, display an overall tendency to form rich intercortical connections, and they are rich in stellate cells that form axons distributed into their dendritic fields as they develop. This dendritic development reduces tissue coorientation as they develop, which could explain the decrease in FA with increasing age. Even deeper layers tend to receive many sensory afferents that often enter the cortex in oblique orientations, which is in contrast to the radially oriented axons exiting into the WM, thereby giving rise to less oriented tissue, which could explain the relatively lower FA on those layers. With increasing intercortical axonal projections and dendritic trees, cortical tissue coorientation ultimately decreases, giving rise to the observed low FA throughout the entire cortex after day 7. Although HR-DTI does not have the resolution to explain precisely the microstructural characteristics that give rise to these observed signal patterns, it agrees very well with our knowledge of the structure of the cortex.

Our results indicate that certain aspects of brain maturation can be measured by DBM at a spatial resolution similar to that of the underlying images, which in the case of this DTI study was 93–120 μm. The high-dimensional image warping method that we have developed had a fundamental role in achieving this localization accuracy because it determined the accuracy of coregistration of brains from different ages, thereby enabling voxel-by-voxel analysis and generation of detailed maps of Figs. 1–3. The achieved coregistration accuracy can be evaluated visually by the anatomical detail shown in the average images in Figs. 1 and 5 and in the regression image in Fig. 2. It has also been validated by experiments. A characteristic example of the spatial resolution of our deformation-based approach is the medial-ventral part of the dhc (see Fig. 2, J), the crisp average images of Figs. 1 and 3 imply overall accurate coregistration of this structure across different mice, despite its very small size relative to the image resolution, thereby enabling the tracking of its change with age. As a result, we measured a pronounced maturation of the dhc, whose FA value almost doubled in the

region proximal to its connection to the hpc. We can hypothesize that the increase in FA in this region is indicative of the strong connectivity between cortical regions and the hpc, mediating memory formation.

HR-DTI obtains an undistorted, spatially consistent 3D volumetric image of the entire brain with high tissue contrast (especially beneficial in early postnatal days) and relatively low human effort, which enables relatively larger-scale brain development studies, compared with histological studies. There is still a tremendous scope of research in HR-DTI in terms of improving the spatial resolution and establishing a direct link between the underlying cellular and molecular processes and the induced (relatively) macroscopic changes in FA and other DT imaging variables, thereby complementing histological and molecular methods.

Although our analysis is now based on relatively small number of mice, we have established the applicability and strength of our automated framework to studies of high resolution DTI. By using our fully automated deformation-based approach, firmer estimates of normal variation of FA, fiber directionality, volume, and other morphological variables measuring aspects of brain growth and maturation will be obtained as our atlas gets populated by additional mice. These normative profiles of change will quantify the normal variation in the morphological phenotype of the mice and reliably distinguish between genetically and environmentally influenced phenotypic abnormalities in brain development, from random intersubject variations. In this analysis, we corroborate the work of several groups [refs. 6–8; see also the Biomedical Informatics Research Network (BIRN) database, available at: www.nbirn.net/testbeds/mouse] that histological, molecular, and MRI methods can have complementary and mutually enhancing roles in understanding normal and abnormal murine brain development.

Our method could also be used for *in vivo* studies. Some examples of these possibilities are (*i*) to determine temporal changes in connectivity or dendritic structure in early postnatal knockout mice, which could then be followed through to maturity (40); (*ii*) to determine the time course and connectivity characterization in the R6/1 mouse model of Huntington's disease in which there is a decrease in dendritic spine morphology, length, and volume of striatal and cortical pyramidal neurons (41); and (*iii*) to track *in vivo* changes in hippocampal cell density and cc in the L1 knockout mice that have abnormal apical dendritic layer (42). Therefore, our framework has the potential to contribute to the greater field of small animal imaging studies that aim at linking the genotype to the phenotype.

This work was supported by the National Institute of Mental Health and National Institute of Biomedical Imaging and Bioengineering Grant R01MH070365.

1. Nolan, P. M., Peters, J., Strivens, M., Rogers, D., Hagan, J., Spurr, N., Gray, I. C., Vizor, L., Brooker, D., Whitehill, E., *et al*. (2000) *Nat. Genet.* **25,** 440–443.
2. Paigen, K. & Eppig, J. T. (2000) *Mamm. Genome* **11,** 715–717.
3. Nakada, T. & Matzuzawa, H. (1995) *Neurosci. Res.* **22,** 389–398.
4. Kooy, R. F., Reyniers, E., Verhoye, M., Sijbers, J., Bakker, C. E., Oostra, B. A., Willems, P. J. &Van Der Linden, A. (1999) *Eur. J. Hum. Genet*. **7,** 526–532.
5. Toga, A. W. T., Santori, E. M., Hazani, R. & Ambach, K. (1995) *Brain Res. Bull.* **38,** 77–85.
6. Johnson, G. A., Cofer, G. P., Gewalt, S. L. & Hedlund, L. W. (2002) *Radiology (Easton, Pa.)* **222,** 789–793.
7. MacKenzie-Graham, A., Lee, E.-F., Dinov, I. D., Bota, M., Shattuck, D. W., Ruffins, S., Yuan, H., Konstantinidis, F., Pitiot, A., Ding, Y., *et al*. (2004) *J. Anat.* **204,** 93–102.
8. Kovacevic, N., Henderson, J. T., Chan, E., Lifshitz, N., Bishop, J., Evans, A. C., Henkelman, R. M. & Chen., X. J. (September 1, 2004) *Cereb. Cortex*, 10.1093/cercor/bhh165.
9. LeBihan, D., Mangin, J.-F., Poupon, C., Clark, C. A., Pappata, S., Molko, N. & Chabriat, H. (2001) *J. Magn. Reson. Imaging* **13,** 534–546.
10. Pierpaoli, C., Jezzard, P., Basser, P. J. & A. Barnett, e. a. (1996) *Radiology (Easton, Pa.)* **201,** 637–648.
11. Huppi, P. S., Maier, S. E., Peled, S., Zientara, G. P., Barnes, P. D., Jolesz, F. A. & Volpe, J. J. (1998) *Pediatr. Res.* **44,** 584–590.
12. Klinberg, T., Vaidya, C. J., Gabrieli, J. D. E., Moseley, M. E. & Hedehus, M. (1999) *NeuroReport* **10,** 2817–2821.
13. Niel, J. J., Shiran, S. I., McKinstry, R. C., Schefft, G. L., Snyder, A. Z., Almli, C. R., Akbudak, E., Aronovitz, J. A., Miller, J. P., Lee, B. C. & Conturo. (1998) *Radiology (Easton, Pa.)* **209,** 57–66.
14. Partridge, S. C., Mukherjee, P., Henry, R. G., Miller, S. P., Berman, J. I., Jin, H., Liu, Y., Glen, O. A., Ferriero, D. M., Barkovich, A. J. & Vigneron, D. B. (2004) *NeuroImage* **22,** 1302–1314.
15. Mori, S., Itoh, R., Zhang, J., Kaufmann, W. E., van Zijl, P. C., Solaiyappan, M. & Yarowsky, P. (2001) *Magn. Reson. Med*. **46,** 18–23.
16. Xue, R., van Zijl, P. C. M., Crain, B. J., Solaiyappan, M. & Mori, S. (1999) *Magn. Reson. Med*. **42,** 1123–1127.
17. Zhang, J., van Zijl, P. C. M. & Mori, S. (2002) *NeuroImage* **15,** 892–901.
18. Baratti, C., Barnett, A. S. & Pierpaoli, C. (1999) *Radiology (Easton, Pa.)* **210,** 133–142.
19. Thompson, P. M., Giedd, J. N., Woods, R. P., MacDonald, D., Evans, A. C. & Toga, A. W. (2000) *Nature* **404,** 190–193.
20. Gogtay, N., Giedd, J. N., Lusk, L., Hayashi, K. M., Greenstein, D., Vaituzis, A. C., Nugent, III, T. F., Herman, D. H., Clasen, L. S., Toga, A. W., *et al*. (2004) *Proc. Natl. Acad. Sci. USA* **101,** 8174–8179.
21. Ashburner, J., Csernansky, J. G., Davatzikos, C., Fox, N. C., Frisoni, G. B. & Thompson, P. M. (2003) *Lancet Neurol.* **2,** 79–88.
22. Thompson, P. M., Vidal, C. N., Giedd, J. N., Gochman, P., Blumenthal, J., Nicolson, R., Toga, A. W. & Rapoport, J. L. (2001) *Proc. Natl. Acad. Sci. USA* **98,** 11650–11655.
23. Shen, D. (2004) in *Proceedings of the 7th International Conference on Medical Image Computing and Computer-Assisted Intervention, Lecture Notes in Computer Science*, eds. Barillot, C., Haynor, D. R. & Hellier, P. (Springer, Berlin), Vol. 3217.
24. Davatzikos, C., Barzi, A., Lawrie, T., Hoon, A. H., Jr., & Melhem, E. R. (2003) *Neuropediatrics* **34,** 247–252.
25. Davatzikos, C. & Resnick, S. M. (2002) *Cereb. Cortex* **12,** 767–771.
26. Resnick, S. M., Goldszal, A., Davatzikos, C., Golski, S., Kraut, M. A., Metter, E. J., Bryan, R. N. & Zonderman, A. B. (2000) *Cereb. Cortex* **10,** 464–472.
27. Resnick, S. M., Pham, D. L., Kraut, M. A., Zonderman, A. B., Davatzikos, C. (2003) *J. Neurosci.* **23,** 3295–3301.
28. Mori, S. & van Zijl, P. C. (1998) *Magn. Reson. Med*. **40,** 511–517.
29. Paxinos, G. & Franklin, K. (2000) *The Mouse Brain in Stereotaxic Coordinates* (Academic, New York).
30. Basser, P. J., Mattiello, J. & LeBihan, D. (1994) *J. Magn. Reson.* **103,** 247–254.
31. Davatzikos, C. (1997) *Comput. Vis. Image Underst.* **66,** 207–222.
32. Shen, D. & Davatzikos, C. (2002) *IEEE Trans. Med. Imaging* **21,** 1421–1439.
33. Xu, D., Mori, S., Shen, D. & Davatzikos, C. (2002) *IEEE Int. Symp. Biomed. Imaging*, 757–760.
34. Xu, D., Mori, S., Shen, D., vanZijl, P. C. M. & Davatzikos, C. (2003) *Magn. Reson. Med*. **50,** 175–182.
35. Davatzikos, C. & Resnick, S. M. (1998) *Cereb. Cortex* **8,** 635–640.
36. Pajevic, C. & Pierpaoli, C. (1999) *Magn. Reson. Med*. **42,** 526–540.
37. Valverde, F. (1967) *Exp. Brain Res.* **3,** 337–352.
38. McKinstry, R. C., Mathur, A., Miller, J. H., Ozcan, A., Snyder, A. Z., Schefft, G. L., Almli, C. R., Shiran, S. I., Conturo, T. E. & Neil, J. J. (2002) *Cereb. Cortex* **12,** 1237–1243.
39. Sholl, D. A. (1956) *The Organization of the Cerebral Cortex* (Hafner, New York); reprinted (1967) (Hafner, New York).
40. Baquet, Z. C., Gorski, J. A. & Jones, K. R. (2004) *J. Neurosci.* **28,** 4250–4258.
41. Spires, T. L., Grote, H. E., Garry, S., Cordery, P. M., Van Dellen, A., Blakemore, C. & Hannan, A. J. (2004) *Eur. J. Neurosci.* **19,** 2799–2807.
42. Demyanenko, G. P., Tsai, A. Y. & Maness, P. F. (1999) *J. Neurosci.* **15,** 4907–4920.